Superiorized Photo-Acoustic Non-NEgative Reconstruction (SPANNER) for Clinical Photoacoustic Imaging

Idan Steinberg, *Member, IEEE*, Jeesu Kim, *Member, IEEE*, Martin K. Schneider, Dongwoon Hyun, *Member, IEEE*, Aimen Zlitni, Sarah M. Hopper, Tal Klap, Geoffrey A. Sonn, Jeremy J. Dahl, *Senior Member, IEEE*, Chulhong Kim, *Senior Member, IEEE*, and Sanjiv Sam Gambhir

***Abstract*— Photoacoustic (PA) imaging can revolutionize medical ultrasound by augmenting it with molecular information. However, clinical translation of PA imaging remains a challenge due to the limited viewing angles and imaging depth. Described here is a new robust algorithm called Superiorized Photo-Acoustic Non-NEgative Reconstruction (SPANNER), designed to reconstruct PA images in real-time and to address the artifacts associated with limited viewing angles and imaging depth. The method utilizes precise forward modeling of the PA propagation and reception of signals while accounting for the effects of acoustic absorption, element size, shape, and sensitivity, as well as the transducer's impulse response and directivity pattern. A fast superiorized conjugate gradient algorithm is used for inversion. SPANNER is compared to three reconstruction algorithms: delay-and-sum (DAS), universal back-projection (UBP), and model-based reconstruction (MBR). All four algorithms are applied to both simulations and experimental data acquired from tissue-mimicking phantoms, *ex vivo* tissue samples, *and in vivo* imaging of the prostates in patients. Simulations and phantom experiments highlight the ability of SPANNER to improve contrast to background ratio by up to 20 dB compared to all other algorithms, as well as a 3-fold increase in axial resolution compared to DAS and UBP. Applying SPANNER on contrast-enhanced PA images acquired from prostate cancer patients yielded a statistically significant difference before and after contrast agent administration, while the other three image reconstruction methods did not, thus highlighting SPANNER's performance in differentiating intrinsic from extrinsic PA signals and its ability to quantify PA signals from the contrast agent more accurately.**

***Index Terms*— Optoacoustic/photoacoustic imaging, prostate, image reconstruction - iterative methods, molecular and cellular imaging.**

Manuscript received November 4, 2020; revised February 25, 2021; accepted March 14, 2021. Date of publication March 23, 2021; date of current version June 30, 2021. This work was supported in part by the Philips Healthcare (S. S. Gambhir and I. Steinberg). The work of Idan Steinberg was supported by the Sir Peter Michael Foundation. The work of Jeesu Kim and Chulhong Kim was supported in part by the National Research Foundation of Korea (NRF) under Grant NRF-2019R1A2C2006269 and Grant NRF-2020R1A6A1A03047902. *(Corresponding author: Idan Steinberg.)*

Idan Steinberg, Martin K. Schneider, Dongwoon Hyun, Aimen Zlitni, and Jeremy J. Dahl are with the Department of Radiology, School of Medicine, Stanford University, Stanford, CA 94305 USA (e-mail: idanstei@stanford.edu; martin.schneider@stanford.edu; dongwoon.hyun@stanford.edu; zlitnia@stanford.edu; jjdahl@stanford.edu).

Jeesu Kim was with the Department of Electrical Engineering, Pohang University of Science and Technology (POSTECH), Pohang 37673, South Korea, and also with the Department of Radiology, School of Medicine, Stanford University, Stanford, CA 94305 USA. He is now with the Department of Cogno-Mechatronics Engineering, College of Nanoscience and Nanotechnology, Pusan National University, Busan 46241, South Korea (e-mail: jeesukim@pusan.ac.kr).

Sarah M. Hopper is with the Department of Electrical Engineering, Stanford University, Stanford, CA 94305 USA (e-mail: smhooper@stanford.edu).

Tal Klap resides in Brooklyn, NY 11211 USA (e-mail: tal_klap@hotmail.com).

Geoffrey A. Sonn is with the Department of Radiology, School of Medicine, Stanford University, Stanford, CA 94305 USA, and also with the Department of Urology, Stanford University, School of Medicine, Stanford University, Stanford, CA 94305 USA (e-mail: gsonn@stanford.edu).

Chulhong Kim is with the Department of Electrical Engineering, Pohang University of Science and Technology (POSTECH), Pohang 37673, South Korea, and also with the Department of Radiology, School of Medicine, Stanford University, Stanford, CA 94305 USA (e-mail: chulhong@postech.ac.kr).

Sanjiv Sam Gambhir, deceased, was with the Department of Radiology, School of Medicine, Stanford University, Stanford, CA 94305 USA.

Digital Object Identifier 10.1109/TMI.2021.3068181

I. Introduction

PHOTOACOUSTIC imaging (PAI), also known as optoacoustic imaging, is a biomedical imaging modality that combines the portability and high resolution of ultrasound imaging (USI) with the molecular contrast and multiplexing capabilities of optical imaging methods [1], [2]. PAI derives its contrast from the optical absorption of tissues. PAI can be implemented in multiscale domains: either in a microscopy configuration [3], which sacrifices imaging depth to achieve micrometer scale resolution or in a tomographic configuration [4], which allows for a few centimeters of imaging depth with ultrasound resolution (typically sub-mm) [5]. Over the past twenty years, the engineering aspects of PAI were thoroughly researched with impressive results obtained mostly for phantom or small animal imaging [6]–[8]. More recently, clinical translation has begun with experimental clinical systems for thyroid cancers [9], lymph node metastasis [10], breast cancers, surgical guidance [11], psoriasis biomarkers [12], or carotid arteries [13]. PAI holds considerable promise for clinical translation with minimal interference to clinical workflow [14], [15] because it can be combined with

conventional USI to provide co-registered anatomical and molecular information [16], [17].

For many PAI technologies, the transition from full-body tomographic imaging in small-animal models to regional clinical human imaging, which allows illumination and detection from only one side, presents new challenges [18]. Such challenges include the limited field of view, degraded signal-to-noise ratio (SNR) due to increased imaging depths, and a requirement for fast processing to allow real-time operation [19]. Moreover, co-registered high-quality USI is invaluable for clinical translation, as it is the standard of care for multiple procedures. Without a clear anatomical image, it is almost impossible to visually segment the image into clinically meaningful regions or find the same region of interest (ROI) in subsequent imaging sessions. Thus, the combination of USI and PAI might seem quintessential; the same transducer can serve as an acoustic emitter for USI as well as an acoustic receiver for both USI and PAI. However, those two modalities often pose different or even conflicting design requirements. USI utilizes small elements [20] (compared to the acoustic wavelength) and flat or convex transducer geometry, while PAI requires large area elements (to increase sensitivity) and concave or tomographic full view transducer geometries.

Despite these hurdles, there is still an essential need for a clinical PAI system that can provide highly accurate and physically faithful image reconstruction in a sufficiently fast (typically 10-20 Hz) manner [18]. Here, we demonstrate a new reconstruction technique, Superiorized Photo-Acoustic Non-Negative Reconstruction (SPANNER), that can provide high quality real-time photoacoustic (PA) image reconstruction even in the presence of limited view and low SNR. This algorithm is based on the concept of mathematical superiorization [21] and is achieved using a detailed model matrix for forward modeling, as well as a superiorized and modified conjugate gradient algorithm for real-time inversion of the model relations. This manuscript compares SPANNER to the two most common image reconstruction algorithms: delay-and-sum (DAS) and universal back-projection (UBP) [22]. Finally, to distinguish the contribution of the SPANNER algorithm from the contribution of the forward model-matrix, we compare it with a model-based reconstruction (MBR) scheme based on a regularized typical least-squares solver [23].

II. The SPANNER Algorithm

The goal of PA image reconstruction is to find $\hat{\mathbf{p}}$, an estimated initial pressure image, given $\mathbf{s}$, a vector of all the measured RF time samples from all detectors and M, pre-calculated forward model matrix that transforms the true image into a noiseless RF: $\mathbf{s} = \mathrm{M}\mathbf{p}$. Additional a-priori constraints must be added to the reconstruction in-lieu of the missing data to negate the effects of noise and limited view. Regardless of the image content, a high-quality PA image should exhibit only nonnegative physical values, clear boundaries, and no signals from optically non-absorptive regions. Thus, proper constraints and regularization are essential for better image qualities. In particular, the anisotropic L^1 total variation (TV) regularization is adapted to enforce desirable image features. TV demonstrates superior performance over classical regularizations [24] since sharp edges are preserved but are not necessarily under- or over-expressed compared to the smooth ones. Instead, the presence of these edges hinges upon the detected signals. However, a non-differentiable L^1 regularization scheme poses challenges for implementation and integration with a conjugate gradient type algorithm. These challenges are exacerbated in a real-time algorithm, where computation efficiency is critical. Thus, we propose using superiorization to perturb a non-linear conjugate gradient algorithm. Superiorization techniques are typically used to improve the efficacy of iterative algorithms in which convergence is resilient to perturbations [21]. Leveraging upon such algorithmic resilience, perturbations can be utilized to steer the algorithm's iterations away from the path that the original algorithm would naively take. The perturbed algorithm is often called the 'superiorized version' of the original unperturbed algorithm. These perturbations force the superiorized algorithm to produce the results that have more desirable attributes compared to the original algorithm, even in the presence of partial or noisy data. Leveraging the work of Zibetti *et al.* [25], we perturbed the non-linear conjugate gradient algorithm to produce a nonnegative, total variation regularized, rapidly converging result. Thus, the problem to be solved for every frame, is:

$$\hat{\mathbf{p}}_{\mathrm{SPNR}} = \underset{\tilde{\mathbf{p}}\geq 0}{\arg\min} \left\{ \|\mathrm{M}\tilde{\mathbf{p}} - \mathbf{s}\|_2^2 + \|\lambda\tilde{\mathbf{p}}\|_2^2 + TV\left(\tilde{\mathbf{p}}\right) \right\} \quad (1)$$

where $\mathbf{p}$ is the initial pressure, M is the model matrix, $\mathbf{s}$ is the raw pressure waveform, and λ is a scalar parameter to control the regularization. The notation $||\cdot||_2$ denotes the L_2 norm of the argument while TV$(\cdot)$ denotes the total variation norm of the argument. Additionally, a precise model matrix was constructed. Succinctly, the model matrix M implements the following relation:

$$s_i\left(t\right) = \frac{\Gamma A_i}{4\pi\, v_s} \left\{ \iiint\limits_{\|\mathbf{r}-\mathbf{d}_i\|_2 = v_s t} \exp\left\{-\alpha\, \|\mathbf{r}-\mathbf{d}_i\|_2\, f_c\right\} \times\; D_i\left(\mathbf{r}-\mathbf{d}_i\right) \frac{\Omega_i\left(\mathbf{r}\right) * p_0\left(\mathbf{r}\right)}{\|\mathbf{r}-\mathbf{d}_i\|_2} d\mathbf{r} \right\} * \frac{\partial h_i\left(t\right)}{\partial t} \quad (2)$$

where Γ is the Grüneisen coefficient, f_c is the detector's central frequency, and α is the acoustic attenuation (in Nepers per unit distance per unit frequency). Each non-ideal detector is characterized by its location $\mathbf{d}_i$, its directivity function $D_i\left(\cdot\right)$, its surface $\Omega_i\left(\mathbf{r}\right) = \begin{cases} 1 & \mathbf{r} \in \text{detector area} \\ 0 & o.w \end{cases}$, its sensitivity A_i, and its impulse response is $h_i\left(t\right)$. By using a two dimensional Cartesian grid and bilinear interpolation, the relation in Eq. 2 can be written in a vector-matrix form. This implementation deviates from the one presented by Rosenthal *et al.* [26]–[28] in the sense that it accounts for the medium properties, the individual element properties of each detector in advance without the need to re-calculate these "on the fly." Finally, the use of a Cartesian grid rather than a triangular grid allows more efficient computation of the total variation regularization.

Overall, SPANNER allows a rapid convergence rate on the order of tens of milliseconds on a graphics processing unit (GPU). Further reduction in computation time was achieved by A) parallel implementation of the algorithms on the GPU, B) use of the Jian, Han & Jiang hybrid coefficient [29] to incorporate computed data from previous iterations to accelerate the next iteration, C) incorporation of data from previous reconstructed images as an initial guess for the algorithm to accelerate the reconstruction of the next image (i.e., hot-start), and D) normalization of the model matrix columns, which is known to accelerate numeric algorithms. A Matlab® code for the SPANNER algorithm can be found online at: github.com/idanstei/Superiorized-PhotoAcoustic-Non-NEgative-Reconstruction-for-Clinical-Photoacoustic-Imaging.

III. Methods

A. In Silico Evaluation

A controlled simulation environment with a well-characterized ground truth was used to compare the DAS, UBP (as implemented in ref [22], Section VI), MBR, and SPANNER. We simulated a 192-element concave array with a 200-micron pitch and 6 mm height. The simulated target was a scaled United States Air Force (USAF) target with an added Stanford University logo in the center (Figure 1a). A forward model matrix was calculated based on the imaging grid (5 cm in depth and 4 cm in azimuth with a 150-μm resolution), acoustic properties of the medium (e.g., speed of sound of 1540 m/s, acoustic attenuation of 0.5 dB/MHz/cm, and Grüneisen coefficient of 0.15), and the detector properties (such as shape, directivity, and sensitivity). Figure 1a shows the forward simulation steps to generate RF data. For forward modeling, the model matrix was applied to the ground truth image, and gaussian white noise was added. Then, each channel was filtered with a 80% bandwidth impulse response function (IRF) as shown in figure 1. This simulated both the effect of the impulse response and in-band noise. Additional white noise was added, and the data was quantized at 14-bit levels. The noise spectral power was varied with respect to the signal power to achieve the desired SNR. Pre-processing for all algorithms included a Wiener deconvolution filter acting on the noisy RF waveforms. In post-processing, nonphysical negative reconstruction values were set to zero for the UBP and MBR algorithms, but no further post-processing steps were taken. The reconstruction performance of each algorithm was evaluated as a function of input RF data SNR, ranging from −9 dB to 20 dB in increments of 3 dB. For each noise level, a total of 200 simulations were performed using random images and noise values. The location of the absorbing pattern shown in Figure 1a was randomly shifted inside the ROI and flipped in both directions to generate different images. Each simulation contained a different realization of random noise, scaled to maintain the specified SNR. The performance was quantified using the root mean square error (also known as the L^2 norm) with respect to the noiseless ground truth image. For each noise level, the mean error and 95% confidence intervals were calculated.

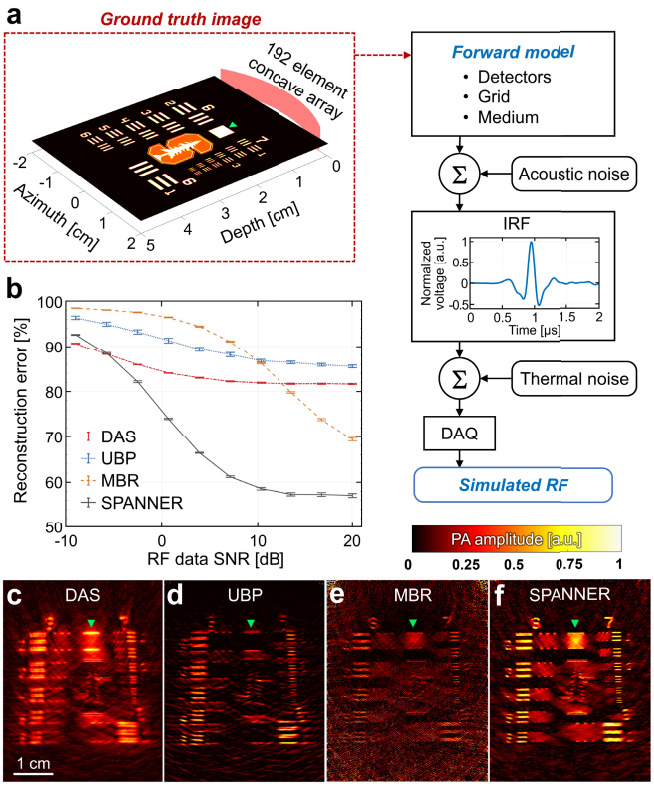

Fig. 1. ***In-silico* comparison of the reconstruction algorithms**. **a (left)** The simulated target based on a scaled standard USAF target with the Stanford logo in the center. A concave array is used to image the target from only one side (right). Forward simulation steps which were taken for generating the simulated RF signals. **b** Comparison of the reconstruction performance of the three algorithms as a function of different SNR of the input RF data. The error is shown with respect to a random guess reconstruction. For each noise level, the average error and 95% confidence intervals are shown. **c-f** DAS, UBP, MBR, and SPANNER reconstructions. Green arrows mark a region of interes.

B. In Vitro Characterization

All algorithms were first evaluated in data previously acquired using a prototype PAI device [30], [31] with a single optical wavelength of 750 nm. The PA signals were acquired using a linear array transducer with 64 elements and a total aperture length of 12.8 mm. The subtended viewing angle at clinically-relevant depths is 65° at 1 cm depth and decreases to less than 15° at 5 cm depth. The impulse response and sensitivity varied greatly between channels and were estimated based on the RF data itself. These were then incorporated into a Weiner-filter pre-processing stage, as well as into the model matrix used by the MBR and SPANNER algorithms. Additionally, the effect of the time-gain-compensation curve was removed during pre-processing from the raw RF data to achieve a constant gain at all depths, as defined by the average intensity across the lateral span. Six black fishing wires (100 micron in diameter) perpendicular to the imaging plane were immersed in water (Fig. 2a). The DAS, UBP, MBR, and SPANNER images were reconstructed from data with identical pre-processing, and the axial resolution was measured as the full-width at half maximum (FWHM).

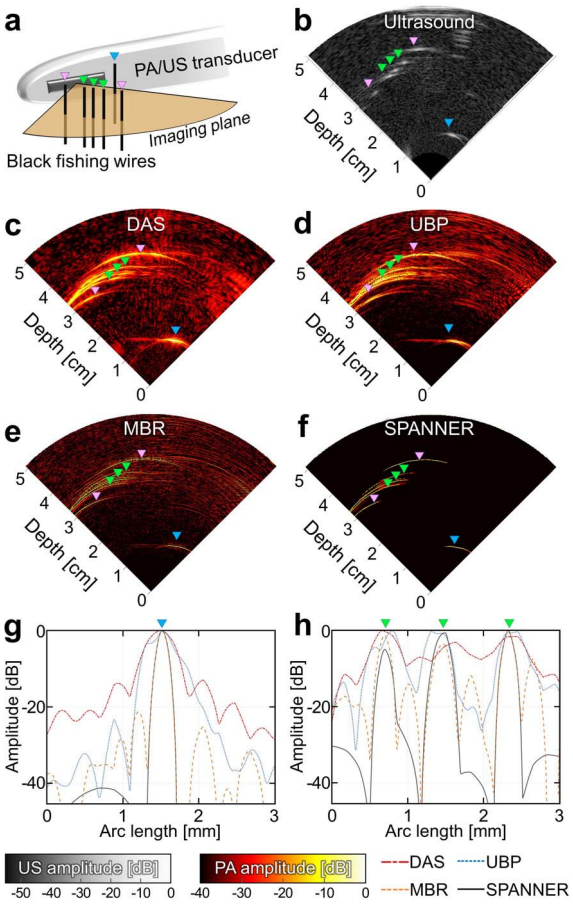

Fig. 2. **Reconstruction of *in vitro* wire-phantom images using a single optical wavelength**. **a** B-mode ultrasound image of the wire phantom. The six wires are marked with colored triangles. **b-e** DAS, UBP, MBR, and SPANNER respective reconstructions. **f,g** Amplitude profiles along a single wire marked with blue and multiple wires marked in green, respectively.

To test the multispectral performance of the SPANNER, we have reanalyzed RF data obtained from a chicken breast phantom experiment [46]. Two pieces of chicken breast (1.8 cm in thickness) were used to sandwich a micro-centrifuge tube containing indocyanine green (ICG) dissolved in PBS at 1.3 mM. PA images were acquired with optical excitation wavelengths ranging from 750 to 950 nm. The amplitude values across the tube were calculated and normalized with respect to the laser power, as well as the adjacent chicken breast surroundings (5 mm below and above the ICG tube) to negate the effect of spectral coloring. The mean and 95% confidence intervals were value calculated as a function of the optical excitation wavelength.

C. Ex Vivo Imaging of Pancreatic Cancers

We reconstructed the PAI data that was previously collected and analyzed during a clinical trial reported by Mallidi *et al.* [47]. In this study, a small cohort of patients (N=7) were injected with 50-100 mg of a functionalized fluorescent agent (panitumumab-IRdye800), which is targeted to the EGFR receptor expressed in pancreatic carcinomas. The confirmed pancreatic cancer patients were injected with the imaging agent 2-5 days prior to fluorescent-guided tumor resection. This period allowed proper agent accumulation at the tumor sites and clearance of the free dye. Following the surgeries, the freshly resected pancreas samples were scanned with both a fluorescence imaging (FLI) system, as well as a custom made PAI system previously reported by our group [46]. Both the FLI and PA images were then correlated to assess the potential of using those modalities for real-time surgical guidance. To ensure the integrity of the samples, they were sandwiched between two agar blocks.

D. In Vivo Imaging of Prostate Cancer Patients

Finally, we assessed the efficacy of these algorithms in reconstructing *in-vivo* PAI data, which were collected using the same device [30]. In this study, PAI RF data were collected from ten patients with suspected prostate cancer lesions who were scheduled for a standard-of-care ultrasound-guided prostate biopsy. These patients were scanned with multiple optical excitation wavelengths (700 nm to 950 nm with a 25 nm interval) before and after systemic injection of FDA-approved ICG contrast agent with doses of 5 to 75 mg in a single bolus injection. Kothapalli *et al.* [46] have recently reported the complete details of this study. Despite the large doses of ICG, the PA images produced in the original work could not demonstrate a statistically significant difference between the images pre- and post-injection ($p > 0.57$ at 800 nm) without resorting to a complicated multi-region, multispectral analysis based on linear unmixing of hemoglobin and ICG. Accurate spectral unmixing remains a significant challenge in PAI [32] due to the absence of multispectral optical fluence compensation [33]. This problem is exacerbated when long measurement times (10-20 minutes per session) introduce motion artifacts and when low SNR and narrow viewing angles skew the reconstruction. Thus, under such conditions, spectral unmixing is inaccurate. To avoid this problem, we chose to focus on a single wavelength of 800 nm close to the ICG peak absorption spectrum (around 790 nm, concentration-dependent). Only the very last image acquired before and immediately after injection were compared. To make the analysis more clinically relevant and to reduce motion artifacts further, we delineated the prostate region in each image manually and quantified the PA signals within the prostate. Then, we used a threshold to reject the lower 10% values within the prostate, thus highlighting blood vessels and regions with high absorbance. We used a two-tailed, paired t-test between the pre- and post-injection images to determine statistical significance. To further assess if the signal increase observed post-injection is attributed to ICG injection and not to any intrinsic contrast or motion artifacts, we analyzed the PA images acquired at 950 nm excitation. Since ICG does not absorb light at 950 nm [34], the images pre- and post- should be statistically equivalent. There are multiple statistical teststo affirm statistical equivalency. The simplest is by using one set of the full overlap of the entire 90% confidence intervals pre- and post-injection to test each reconstruction's ability to quantify a lack of change. For a fair comparison, the PA images presented from this study

were jointly normalized to a 40 dB range for both pre- and post-injection images, the amplitude of the PA signal is presented with respect to the maximal amplitude post-injection with the same optical excitation wavelength of 800 nm. All analyses were performed on the linear scale values. Finally, we analyzed the PA amplitude as a function of the ICG dose injected into each patient. As the signal value changes significantly from patient to patient, we calculated the ratio (i.e., mean PA amplitude in the prostate post-injection divided by the same amplitude pre-injection). These ratios were plotted (best fit and 90% prediction bounds) as a function of the dose for each of the four algorithms.

E. GPU Implementation of SPANNER

The SPANNER requires heavy computations for real-time operation. Simultaneous co-localized USI and PAI were implemented for GPU-based execution on a single high-end GPU (Nvidia, Quadro GV-100, USA) based on a modified open-source GPU beamforming package by Hyun *et al.* [35]. USI was performed using a diverging-beam, coherently compounded synthetic aperture sequence, and PAI was performed using the SPANNER algorithm. The algorithm was implemented as a set of CUDA kernels based on cuBLAS-V2 and cuSPARSE libraries. Computations were further accelerated by using the Jian, Han, & Jiang hybrid coefficient [29] to incorporate computed data from previous iterations to speed up the next iteration, and by using previously-reconstructed images as an initial guess for the algorithm to accelerate the reconstruction of the following image (i.e., hot-start). Finally, an optional pre-processing step of frequency Wiener filtering was implemented in the frequency domain using the cuFFT library for Fast Fourier Transforms. The CUDA implementation also normalized and log-compressed the images as necessary as well as extracted timestamps and maximal values for both PA and US images.

IV. Results

A. In Silico Evaluation

The *in silico* evaluation results are shown in Figure 1. Figure 1a shows the simulated phantom and the forward generation of RF. Figure 1b shows the RMS reconstruction errors compared to the ground truth image. The error was normalized with respect to the error from a random guess.

Due to the limited view angle, spatial frequencies in the azimuthal direction cannot be fully recovered by any of the algorithms. As expected, all algorithms performed better as the SNR of the input RF data increases. However, as the SNR improves, the artifacts due to the limited view become dominant and hamper further reduction in the reconstruction error. The SPANNER produces the most accurate result for the most input noise levels. Accuracy is improved up to 3-fold compared to DAS and UBP at the high SNR and up to 7-fold compared to MBR at the low and mid-range SNRs. Figures 1c-f show an example of the reconstructed images with an input SNR of 4 dB. The DAS algorithm severely smears the image, and the image values are not quantitative as the lower spatial frequencies (i.e., the baseline) are missing. This means that the pixel values do not scale with the actual absorption. One can observe that the full rectangle in the upper region (marked with a green triangle) appears as two boundaries with minimal signal inside, instead of accentuating the proximal and distal edges. The UBP algorithm exhibits much less smearing in the axial direction but still fails to reconstruct the lower frequency content. While the MBR was able to achieve a more quantitative reconstruction close to the detector array, it is severely hampered by the noise, and the reconstructed image is very unclear at depth. In contrast, the SPANNER was able to reconstruct both clear boundaries and preserve the feature's inner filling accurately, although there is some smearing in the lateral direction.

B. In Vitro Characterization

The *in vitro* imaging results using a single optical wavelength are presented in Figure 2. Figure 2a depicts the experimental setup, and Figure 2b shows a conventional B-mode ultrasound image of the wires, each marked with a colored triangle. The images produced by all four algorithms are shown in Figures 2c-f. Both DAS and UBP demonstrate low resolution (both axial and lateral) and a high background noise clutter (i.e., spurious signals). The MBR algorithm also suffers from a high spurious background. While the SPANNER algorithm could not improve the lateral resolution, it had a much higher axial resolution and improved the signal to background ratio.

We quantitatively compared the cross-sectional PA amplitude profiles across the wire marked with a blue triangle (Fig. 2g). Each amplitude profile was normalized to the peak value. The axial resolutions of the DAS and UBP (465 μm) are almost three times worse than that of SPANNER and MBR (165 μm). While the MBR was more successful in rejecting the background noise compared to the UBP, the SPANNER markedly outperforms all algorithms and significantly reduces the background noise by at least 40 dB (an order of magnitude better than DAS). Figure 2h illustrates the separability of multiple point targets using the amplitude profiles through the three tightly packed wires ($\sim$1 mm apart) marked with green triangles. The DAS failed to detect the center point target, whereas the UBP, MBR, and SPANNER resolved all three distinct points. The SPANNER and MBR retained a markedly better axial resolution in contrast to the DAS and UBP. However, the MBR algorithm, while outperforming the DAS and UBP, generated multiple spurious artifacts that prevented proper image quantification and reduced the contrast and thus was also limited to a dynamic range of 20 dB or less. The SPANNER provides an additional 15-20 dB of dynamic range and allows a more physically accurate reconstruction.

Figure 3 demonstrates the multispectral performance of the four reconstruction algorithms. The ICG tube was located between two chicken breast tissues (Figure 3a) and was confirmed in the B-mode US image (Figure 3b). The multispectral PA amplitudes processed using the four reconstruction algorithms were calculated in Figure 3c. The known, normalized absorption spectra of ICG with the same concentration [34] is

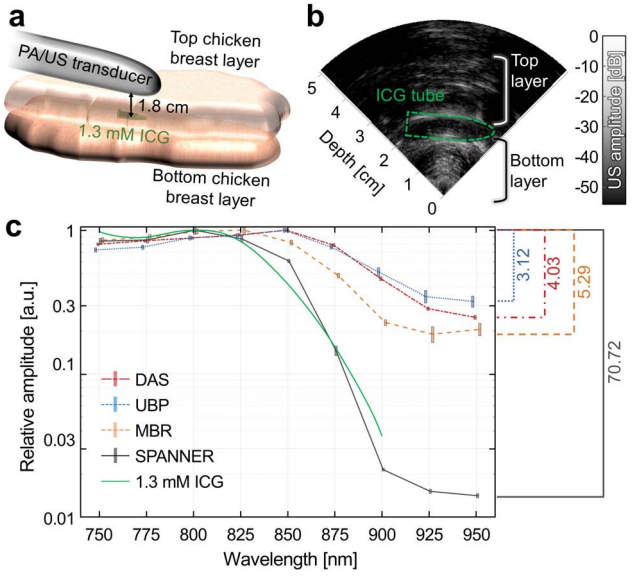

Fig. 3. **Multispectral reconstruction of an ICG tube in chicken breast tissues *in vitro*.** **a** The experimental setup - an ICG tube was sandwiched between two pieces of thick chicken breasts. **b** B-mode ultrasound image showing the ICG tube and chicken breast layers. **c** **The** DAS, UBP, MBR, and SPANNER PA spectra vs. the actual ICG absorption spectrum. The values shown are average across all pixels ± 95% confidence intervals.

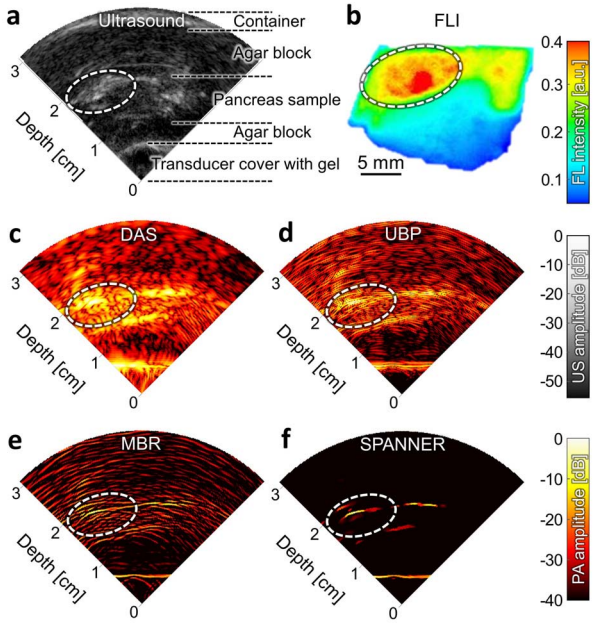

Fig. 4. **Ultrasound (US), fluorescence (FL), and photoacoustic (PA) *ex vivo* images of pancreatic cancer samples**. **a** US image of the tissue sample sandwiched between two agar blocks. **b** FLI heatmap of a part of the pancreases tissue sample, showing the high signal in the tumor region. **c-f** PA image of the same tissue sample produced by the DAS, UBP, MBR, and SPANNER reconstructions, respectively.

included as a reference. Both the DAS and UBP algorithms fail to track the ICG spectrum accurately.

Moreover, the dynamic range, i.e., the change in absorption between peak and lowest absorption, is limited to a 3-fold for the UBP and 4-fold for the DAS. The MBR performed slightly better with a dynamic range of 5-fold. In contrast, The SPANNER produces accurate quantitative measurements that correlate well with the ICG absorption spectrum at 1.3 mM. Furthermore, the dynamic range of the SPANNER is more than an order of magnitude better (∼71-fold) than all other algorithms.

C. Ex Vivo Imaging of Pancreatic Cancers

Clinically excised pancreatic cancer samples were ultrasonically (Fig. 4a), fluorescently (Fig. 4b), and photoacoustically (Figs. 4c–f) imaged. The tissue samples were sandwiched between two blocks of agar. The boundary of the pancreatic cancer sample was confirmed by histopathology.

The tissue sample was shown to be highly fluorescent when excited at 780 nm, and the tumor region is marked with a dashed line (Fig. 4b). The PA images processed using the DAS, UBP, MBR, and SPANNER (Figs. 4c–f, respectively) are shown in the log scale with a 40-dB dynamic range. The bright signals were observed at the bottom of each of the PA images, mainly due to the suboptimal acoustic and optical coupling between the gel-filled transducer cover and the agar blocks. Otherwise, all PA reconstruction algorithms were able to detect the FLI contrast agent successfully and showed a good correlation with FLI. As expected, the DAS, UBP, and MBR fail to entirely reject noise and undesired signals from the clear agar blocks surrounding the sample, leading to a 10-fold (20 dB) decrease, in contrast, relative to the SPANNER.

D. In Vivo Imaging of Prostate Cancers

The *in vivo* PAI data acquired from the patients with suspected prostate cancer are shown in Fig. 5. An exemplary US B-mode image delineates a rectal wall (R), prostate (P), connective tissue (C), and bladder (B) (Fig. 5a). The PA images were reconstructed using all four algorithms pre- (Figs. 5d–g) and post-injection (Figs. 5h–k). The PA amplitudes estimated with all four algorithms are quantitatively compared before and after the injection of ICG at 800 nm. This wavelength allows the maximal PA signal due to the peak ICG absorption. As shown in Fig. 5b, all methods demonstrated a mean increase in PA amplitude (DAS, 5.4%; UBP, 6.4%; MBR, 6.5%; and SPANNER, 59.5%), but the DAS, UBP, and MBR failed to produce any statistically significant difference (p-values of 0.25, 0.13 and 0.08 respectively). In contrast, the SPANNER was able to demonstrate a statistically significant difference in quantitative PA value before and after injection (p-value < 0.04). To further confirm whether the PA signal increase after ICG injection is attributed to ICG injection, to any intrinsic contrast, or motion artifacts, we analyzed the spectral PA response at another wavelength, 950 nm, where no ICG absorbs light. The SPANNER only generated the PA signals with a full overlap of the confidence intervals, and thus showing statistically significant equivalency between two PA signals before and after injection at 950 nm (Fig. 5c).

When comparing a set of exemplary PA images before (Figs. 5d-g) and after (Figs. 5h-k) ICG injection (25 mg), we qualitatively observed a slight increase in PA amplitude between those images reconstructed using the four different algorithms. These differences are further pronounced in the

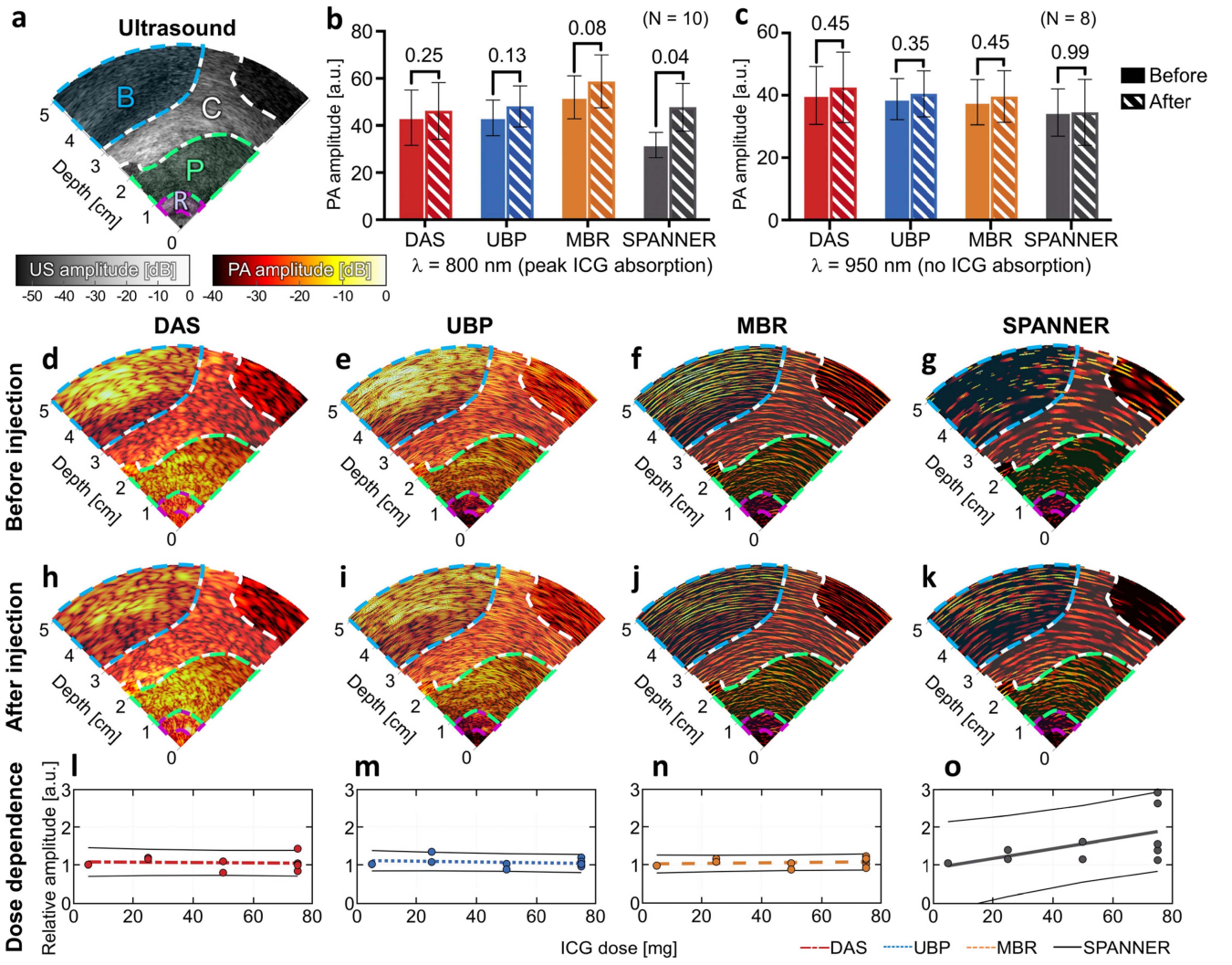

Fig. 5. **PA image reconstruction and quantification of prostate cancers *in vivo*.** **a**. B-mode US image for anatomical reference. The rectal wall (R), prostate (P), connective tissue (C), and bladder (B) are delineated with dotted lines. **b**. Quantified PA amplitudes at the Prostate regions before and after injection of ICG at 800 nm (N = 10). Paired t-test showing that the SPANNER only achieved a statistically significant difference ($p = 0.04$). **c**. Quantified PA amplitudes of the prostate before and after injection of ICG at 950 nm (N = 8). **d-g**. Exemplary DAS, UBP, MBR, and SPANNER reconstruction of the pre-injection PA image at 800 nm. **h-k**. PA images of the same patient immediately after injection of 25 mg of ICG. **i-o**. Relative PA amplitudes within the prostate (post-injection amplitude divided by pre-injection amplitude) as a function of ICG dose for the DAS, UBP, MBR, and SPANNER algorithms, respectively. Colored thick lines show linear regression; thin black lines show 90% prediction bounds.

SPANNER images. Further, the background noises are prominent in the DAS, UBP, and MBR images, while the noises are significantly suppressed in the SPANNER image.

Finally, we plotted the normalized PA values as a function of the ICG dose at 800 nm. Since there were only a few patients for each dose (one to five patients per dose), the confidence intervals are broad. Nevertheless, only the SPANNER produces a trend sensitive to the ICG dose. The slope of SPANNER (12.85 g^{-1} ICG) was 12 to 28 times higher than any other method (−0.46, −1.03, and 1.76 g^{-1}ICG for the DAS, MBR, and UBP respectively).

E. GPU Implementation of the SPANNER

The GPU implementation was able to reconstruct both PA and US images with a clinically-relevant image grid (5 cm in depth and 4 cm in azimuth with a 135-micron pixel size) in ∼90 milliseconds. This reconstruction time includes all overhead, including the transfer of data from Matlab to the GPU and back. For PAI alone, the SPANNER was able to achieve ∼45 milliseconds of computation time per frame. Such a rate allows for a frame rate higher than 11 frames per second for combined PAI and USI or 22 frames per second for PAI alone.

V. Discussion

We describe a novel algorithm for PA image reconstruction called SPANNER. This algorithm was explicitly designed to overcome the existing hurdles for clinically realistic PAI, which consists of limited viewing angles and high noise, and to enable real-time imaging. The proposed algorithm leverages a model-based approach [26] for forward modeling that is combined with the concept of mathematical superiorization [21]. Unlike a simple, conjugate gradient algorithm that solves the

linear model matrix equation, our proposed algorithm enforces nonnegativity and anisotropic total variation regularization that results in robustness to noise and physically accurate images. This algorithm was thoroughly compared with both the DAS and UBP beamforming methods, two of the most widely-used algorithms in biomedical PAI [36]. Additionally, the SPANNER algorithm was also compared to a model-based approach (MBR) using the same forward model matrix as SPANNER but with Tikonov L^2 regularization and a conjugate gradient algorithm. Because clinical translation is our primary focus, SPANNER is more compatible with clinical transducers and PA tomography.

Based on the *in-silico* and *in vitro* results, the SPANNER algorithm can improve axial resolution by up to 3-fold and contrast by up to an order of magnitude. The SPANNER provided a more quantitative reconstruction and was shown to quantify the ICG absorption spectrum properly and achieved a 15-30 fold higher dynamic range. Thus, the proposed algorithm represents a significant improvement toward clinical translation of PAI. Applying SPANNER to *ex-vivo* patient sample data showed a high correlation with fluorescence signals and better rejection of the background. Statistical analysis of *in-vivo* data showed the improved ability of SPANNER to distinguish between images before and after ICG injection. This will allow for better diagnostic capabilities and reducing the agent dosage.

While SPANNER demonstrated impressive performance, it is also prone to several difficulties. The first and most important hurdle is its strong dependence on an accurate forward model matrix. The model matrix used in SPANNER describes the relationship between the image to be estimated and the (noiseless) RF signals to be measured. The model matrix can be calculated in advance and incorporates data regarding the transducer properties and the geometry of imaging. We did not optimize the speed of sound or acoustic attenuation and used standard values from the literature (1540 m/s and 0.5 dB/MHz/cm). It might be the case that better tuning of these values will result in improved images, but from our experience, there is low sensitivity to the exact value chosen as errors from the limited view and low SNR overwhelm these inaccuracies. However, inaccuracies in the model matrix will lead to artifacts in image reconstruction. We did not evaluate the degradation in performance with respect to the model matrix inaccuracies; however, considerable inaccuracies might cause reconstruction errors that overwhelm the true image features and would make it unusable. In that regard, the DAS algorithm, and its variants [19], only requires the exact location of each transducer element with respect to each pixel, which is more straightforward to implement. However, the model matrix only needs to be calculated once. Because all the required data needed for the calculation can be collected in advance by simple hydrophone measurements, we do not consider data availability to be a significant hurdle.

While SPANNER can better utilize the raw RF data to form a more accurate image, it cannot generate missing data due to the limited viewing angles. A transducer optimized for ultrasound imaging (and especially phased-array where the aperture is typically small) would provide poor PAI regardless of the algorithm used for reconstruction. Such is the case for the device that was used for the current study. It is evident in the wire-phantom experiments where the axial resolution was improved three-fold, but the lateral resolution remained poor. Better design of the transducer array (such as a large aperture or a concave array) is required in order to negate the effects of the limited view [37]. It should be noted that only one transducer was used for this study. It is hard to estimate the improvement in performance for a system fully optimized for PAI that sacrifices co-registered USI and clinical applicability. A minor caveat to the proposed SPANNER method is the assumption of nonnegativity. As long as the medium of interest is characterized by a positive Grüneisen coefficient (which is the case for all native tissue components under physiological conditions), a nonnegativity constraint can improve results. However, under certain extreme conditions (such as very low temperatures [38] and for some unusual contrast agents [39]), a negative Grüneisen may be encountered. Under these conditions, the nonnegativity constraint can be removed from the algorithm by a simple modification of the projected estimate, but this can adversely affect the algorithm's performance. Further work is required to assess the impact of such a change. Finally, since SPANNER provides acoustic reconstruction only (i.e., estimation of the initial pressure and not of the actual absorption), compensation of the fluence remains a significant challenge in PAI [32] and, to the best of our knowledge, is not yet addressed by any generalizable algorithm. However, because SPANNER provides a more accurate acoustic reconstruction of the initial pressure compared to other commonly used algorithms, it provides a better starting point to build upon for any further offline analysis that attempts at compensating for the fluence variations.

Lastly, the computation time is vital for the clinical utilization of SPANNER. With a proper implementation on a single GPU, SPANNER can achieve a frame rate greater than 20 frames per second (or ten frames per second combined with high-end USI). Because many Q-switched nanosecond lasers used for deep tissue PAI are limited to 10 pulses per second, this is not a significant hurdle. Moreover, this frame rate is sufficiently fast for many clinical applications. Algorithms like DAS enjoy a simple closed-form structure that allows the calculation of all required parameters during imaging. Thus, it can be adapted to many imaging configurations with no prior preparations. In contrast, SPANNER relies on a forward model matrix that needs to be computed and stored in advance. The offline computation of the model matrix can take at least several hours. Such calculation can be accelerated as well by a proper GPU implementation; moreover, it is only required once per experimental setting. For example, all results in this paper were achieved using only three distinct model matrices: one for the simulation of a 192 element transducer, one for the clinical device in water (wire phantom), and one for the same device in patients (where the speed of sound was set to 1540 m/s). Recent research suggests that the computation of the model matrix might also be performed in real-time during imaging by utilizing some approximations [40], which might allow easier adaptation of SPANNER.

The implications of more quantitative images *in-vivo* are far-reaching. Clinical translation of PAI has just begun in recent years [18]; however, almost every clinical application that requires an imaging depth of more than a few mm and relies on optical absorption contrast can benefit from the increase in accuracy and lower background levels. Applications like image-guided surgery [41] and visual servoing [42] can immediately benefit from SPANNER to better pinpoint surgical tools and major blood vessels, which is not achievable with the DAS due to his background noise [42]. Moreover, endogenous contrast might not be sufficient to provide clinicians with molecular data related to disease location and progression [43]. Thus, exogenous contrast agents (mostly likely functionalized small molecules), in combination with clinical PAI, can provide a wealth of molecular information with applications for biopsy guidance [44], detection of cancer [45], and triaging [46] as well as monitoring of tumor recurrence and treatment efficacies [47]. The increased sensitivity provided by the SPANNER can help minimize the injected dose required for reliable imaging, potentially reducing any adverse toxicities from the contrast agents and allowing more frequent imaging that can significantly assist in the clinical translation of PAI.

Further work is required to integrate SPANNER in clinical imaging workflow fully. Both the pre-processing Weiner filter and the main algorithm have multiple parameters to control their behavior (such as the number of iterations, tolerance for convergence, and level of noise rejection). The full optimization of those parameters depend on the specific geometry, detector sensitivity, and target to be imaged will further improve SPANNER performance. Finally, the current algorithm allows for 2D imaging and not full 3D tomography. Adaptation of the SPANNER algorithm itself for 3D applications is straightforward and mainly involves modification of the fast gradient projection [48] section. However, the forward model matrix also needs to be updated. Its memory size might grow considerably (10-100 fold) in such a manner that it will not allow real-time applications. For many clinical applications, a single 2D image or a stack of images that emulate the full 3D data are sufficient, but further investigation is required [49].

To conclude, this work presents a new approach for the reconstruction of PA images with markedly better accuracy, resolution, and dynamic range compared to all other algorithms. It is specifically designed for clinical PAI applications in which there is limited viewing angle and low SNR at depth. Real-time application of SPANNER can open avenues for clinical translation of PAI for an abundance of applications.

Acknowledgment

The authors would like to dedicate this work to the memory and legacy of Professor S. S. Gambhir.

References

[1] P. Beard, "Biomedical photoacoustic imaging," *Interface Focus*, vol. 1, no. 4, pp. 602–631, Aug. 2011.

[2] G. P. Luke, D. Yeager, and S. Y. Emelianov, "Biomedical applications of photoacoustic imaging with exogenous contrast agents," *Ann. Biomed. Eng.*, vol. 40, no. 2, pp. 422–437, Feb. 2012.

[3] K. Maslov, H. F. Zhang, S. Hu, and L. V. Wang, "Optical-resolution photoacoustic microscopy for *in vivo* imaging of single capillaries," *Opt. Lett.*, vol. 33, no. 9, pp. 929–931, 2008.

[4] X. Wang, Y. Pang, G. Ku, X. Xie, G. Stoica, and L. V. Wang, "Noninvasive laser-induced photoacoustic tomography for structural and functional *in vivo* imaging of the brain," *Nature Biotechnol.*, vol. 21, no. 7, pp. 803–806, Jul. 2003.

[5] W. Choi, E.-Y. Park, S. Jeon, and C. Kim, "Clinical photoacoustic imaging platforms," *Biomed. Eng. Lett.*, vol. 8, no. 2, pp. 139–155, May 2018.

[6] M. Jeon, J. Kim, and C. Kim, "Multiplane spectroscopic whole-body photoacoustic imaging of small animals *in vivo*," *Med. Biol. Eng. Comput.*, vol. 54, nos. 2–3, pp. 283–294, Mar. 2016.

[7] A. P. Jathoul *et al.*, "Deep *in vivo* photoacoustic imaging of mammalian tissues using a tyrosinase-based genetic reporter," *Nature Photon.*, vol. 9, no. 4, p. 239, 2015.

[8] J. Staley, P. Grogan, A. K. Samadi, H. Cui, M. S. Cohen, and X. Yang, "Growth of melanoma brain tumors monitored by photoacoustic microscopy," *J. Biomed. Opt.*, vol. 15, no. 4, 2010, Art. no. 040510.

[9] A. Dima and V. Ntziachristos, "*In-vivo* handheld optoacoustic tomography of the human thyroid," *Photoacoustics*, vol. 4, no. 2, pp. 65–69, Jun. 2016.

[10] I. Stoffels *et al.*, "Metastatic status of sentinel lymph nodes in melanoma determined noninvasively with multispectral optoacoustic imaging," *Sci. Transl. Med.*, vol. 7, pp. 199–317, Dec. 2015.

[11] A. Horiguchi *et al.*, "A pilot study of photoacoustic imaging system for improved real-time visualization of neurovascular bundle during radical prostatectomy," *Prostate*, vol. 76, no. 3, pp. 307–315, Feb. 2016.

[12] J. Aguirre *et al.*, "Precision assessment of label-free psoriasis biomarkers with ultra-broadband optoacoustic mesoscopy," *Nature Biomed. Eng.*, vol. 1, no. 5, p. 0068, May 2017.

[13] A. Dima and V. Ntziachristos, "Non-invasive carotid imaging using optoacoustic tomography," *Opt. Exp.*, vol. 20, no. 22, pp. 25044–25057, 2012.

[14] K. E. Wilson, T. Y. Wang, and J. K. Willmann, "Acoustic and photoacoustic molecular imaging of cancer," *J. Nucl. Med.*, vol. 54, no. 11, pp. 1851–1854, Nov. 2013.

[15] S. Zackrisson, S. M. W. Y. van de Ven, and S. S. Gambhir, "Light in and sound out: Emerging translational strategies for photoacoustic imaging," *Cancer Res.*, vol. 74, no. 4, pp. 979–1004, Feb. 2014.

[16] R. G. M. Kolkman, P. J. Brands, W. Steenbergen, and T. G. van Leeuwen, "Real-time *in vivo* photoacoustic and ultrasound imaging," *J. Biomed. Opt.*, vol. 13, no. 5, 2008, Art. no. 050510.

[17] K. Daoudi *et al.*, "Handheld probe integrating laser diode and ultrasound transducer array for ultrasound/photoacoustic dual modality imaging," *Opt. Exp.*, vol. 22, no. 21, pp. 26365–26374, 2014.

[18] I. Steinberg, D. M. Huland, O. Vermesh, H. E. Frostig, W. S. Tummers, and S. S. Gambhir, "Photoacoustic clinical imaging," *Photoacoustics*, vol. 14, pp. 77–98, Jun. 2019.

[19] S. Jeon, E.-Y. Park, W. Choi, R. Managuli, K. J. Lee, and C. Kim, "Real-time delay-multiply-and-sum beamforming with coherence factor for *in vivo* clinical photoacoustic imaging of humans," *Photoacoustics*, vol. 15, Sep. 2019, Art. no. 100136.

[20] T. L. Szabo, *Diagnostic Ultrasound Imaging: Inside Out*. New York, NY, USA: Academic, 2004.

[21] Y. Censor, G. T. Herman, and M. Jiang, "Superiorization: Theory and applications," *Inverse Problems*, vol. 33, no. 4, Apr. 2017, Art. no. 040301.

[22] M. Xu and L. V. Wang, "Universal back-projection algorithm for photoacoustic computed tomography," *Phys. Rev. E, Stat. Phys. Plasmas Fluids Relat. Interdiscip. Top.*, vol. 71, no. 1, Jan. 2005, Art. no. 016706.

[23] C. C. Paige and M. A. Saunders, "LSQR: An algorithm for sparse linear equations and sparse least squares," *ACM Trans. Math. Softw.*, vol. 8, no. 1, pp. 43–71, Mar. 1982.

[24] D. Van de Sompel, L. S. Sasportas, J. V. Jokerst, and S. S. Gambhir, "Comparison of deconvolution filters for photoacoustic tomography," *PLoS ONE*, vol. 11, no. 3, Mar. 2016, Art. no. e0152597.

[25] M. V. W. Zibetti, C. Lin, and G. T. Herman, "Total variation superiorized conjugate gradient method for image reconstruction," *Inverse Problems*, vol. 34, no. 3, Mar. 2018, Art. no. 034001.

[26] A. Rosenthal, D. Razansky, and V. Ntziachristos, "Fast semi-analytical model-based acoustic inversion for quantitative optoacoustic tomography," *IEEE Trans. Med. Imag.*, vol. 29, no. 6, pp. 1275–1285, Jun. 2010.

[27] X. L. Deán-Ben, R. Ma, A. Rosenthal, V. Ntziachristos, and D. Razansky, "Weighted model-based optoacoustic reconstruction in acoustic scattering media," *Phys. Med. Biol.*, vol. 58, no. 16, p. 5555, 2013.

[28] X. L. Deán-Ben, A. Buehler, V. Ntziachristos, and D. Razansky, "Accurate model-based reconstruction algorithm for three-dimensional optoacoustic tomography," *IEEE Trans. Med. Imag.*, vol. 31, no. 10, pp. 1922–1928, Oct. 2012.

[29] J. Jian, L. Han, and X. Jiang, "A hybrid conjugate gradient method with descent property for unconstrained optimization," *Appl. Math. Model.*, vol. 39, nos. 3–4, pp. 1281–1290, Feb. 2015.

[30] S.-R. Kothapalli *et al.*, "Simultaneous transrectal ultrasound and photoacoustic human prostate imaging," *Sci. Transl. Med.*, vol. 11, no. 507, 2019, Art. no. eaav2169.

[31] W. S. Tummers *et al.*, "Intraoperative pancreatic cancer detection using tumor-specific multimodality molecular imaging," *Ann. Surgical Oncol.*, vol. 25, no. 7, pp. 1880–1888, Jul. 2018.

[32] B. Cox, J. G. Laufer, S. R. Arridge, and P. C. Beard, "Quantitative spectroscopic photoacoustic imaging: A review," *J. Biomed. Opt.*, vol. 17, no. 6, 2012, Art. no. 061202.

[33] S. Tzoumas, N. Deliolanis, S. Morscher, and V. Ntziachristos, "Unmixing molecular agents from absorbing tissue in multispectral optoacoustic tomography," *IEEE Trans. Med. Imag.*, vol. 33, no. 1, pp. 48–60, Jan. 2014.

[34] M. L. Landsman, G. Kwant, G. A. Mook, and W. G. Zijlstra, "Light-absorbing properties, stability, and spectral stabilization of indocyanine green," *J. Appl. Physiol.*, vol. 40, no. 4, pp. 575–583, Apr. 1976.

[35] D. Hyun, Y. L. Li, I. Steinberg, M. Jakovljevic, T. Klap, and J. J. Dahl, "An open source GPU-based beamformer for real-time ultrasound imaging and applications," in *Proc. IEEE Int. Ultrason. Symp. (IUS)*, Oct. 2019, pp. 20–23.

[36] A. Rosenthal, V. Ntziachristos, and D. Razansky, "Acoustic inversion in optoacoustic tomography: A review," *Current Med. Imag. Rev.*, vol. 9, no. 4, pp. 318–336, Jan. 2014.

[37] M. W. Schellenberg and H. K. Hunt, "Hand-held optoacoustic imaging: A review," *Photoacoustics*, vol. 11, pp. 14–27, Sep. 2018.

[38] K. V. Larin, I. Larina, M. Motamedi, and R. Esenaliev, "Optoacoustic laser monitoring of cooling and freezing of tissues," *Quantum Electron.*, vol. 32, no. 11, p. 953, 2002.

[39] E. Petrova, A. Liopo, A. A. Oraevsky, and S. A. Ermilov, "Temperature-dependent optoacoustic response and transient through zero Grüneisen parameter in optically contrasted media," *Photoacoustics*, vol. 7, pp. 36–46, Sep. 2017.

[40] L. Ding, X. L. Deán-Ben, and D. Razansky, "20 frames per second model-based reconstruction in cross-sectional optoacoustic tomography," *Proc. SPIE*, vol. 10064, Mar. 2017, Art. no. 100641A.

[41] I. S. Alam *et al.*, "Emerging intraoperative imaging modalities to improve surgical precision," *Mol. Imag. Biol.*, vol. 20, no. 5, pp. 705–715, Oct. 2018.

[42] M. A. L. Bell and J. Shubert, "Photoacoustic-based visual servoing of a needle tip," *Sci. Rep.*, vol. 8, no. 1, pp. 1–12, Dec. 2018.

[43] P. J. van den Berg, K. Daoudi, H. J. B. Moens, and W. Steenbergen, "Feasibility of photoacoustic/ultrasound imaging of synovitis in finger joints using a point-of-care system," *Photoacoustics*, vol. 8, pp. 8–14, Dec. 2017.

[44] C. Kim *et al.*, "Handheld array-based photoacoustic probe for guiding needle biopsy of sentinel lymph nodes," *J. Biomed. Opt.*, vol. 15, no. 4, 2010, Art. no. 046010.

[45] K. S. Valluru, K. E. Wilson, and J. K. Willmann, "Photoacoustic imaging in oncology: Translational preclinical and early clinical experience," *Radiology*, vol. 280, no. 2, pp. 332–349, Aug. 2016.

[46] J. Kim *et al.*, "Multispectral photoacoustic assessment of thyroid cancer nodules *in vivo*," *Proc. SPIE*, vol. 11240, Feb. 2020, Art. no. 1124004.

[47] S. Mallidi, K. Watanabe, D. Timerman, D. Schoenfeld, and T. Hasan, "Prediction of tumor recurrence and therapy monitoring using ultrasound-guided photoacoustic imaging," *Theranostics*, vol. 5, no. 3, p. 289, 2015.

[48] A. Beck and M. Teboulle, "Fast gradient-based algorithms for constrained total variation image denoising and deblurring problems," *IEEE Trans. Image Process.*, vol. 18, no. 11, pp. 2419–2434, Nov. 2009.

[49] C. Lee, W. Choi, J. Kim, and C. Kim, "Three-dimensional clinical handheld photoacoustic/ultrasound scanner," *Photoacoustics*, vol. 18, Jun. 2020, Art. no. 100173.